CCFE
CULHAM CENTRE FOR FUSION ENERGY

UK Atomic Energy Authority

UKAEA-CCFE-PR(19)04

S. Buller, H.M. Smith, A. Mollen, S.L. Newton, I. Pusztai

# Transport of collisional impurities with flux-surface density variation in stellarator plasmas

# Transport of collisional impurities with flux-surface density variation in stellarator plasmas

S. Buller, H.M. Smith, A. Mollen, S.L. Newton, I. Pusztai

This is a preprint of a paper submitted for publication in
Nuclear Fusion

# Transport of collisional impurities with flux-surface density variation in stellarator plasmas

S. Buller,[1, a)] H.M. Smith,[2] A. Mollén,[2] S.L. Newton,[3, 1] and I. Pusztai[1]
[1)] *Department of Physics, Chalmers University of Technology, SE-41296 Göteborg, Sweden*
[2)] *Max-Planck-Institut für Plasmaphysik, 17491 Greifswald, Germany*
[3)] *CCFE, Culham Science Centre, Abingdon, Oxon OX14 3DB, UK*

(Dated: 20 December 2018)

Avoiding impurity accumulation is a requirement for steady-state stellarator operation. The accumulation of impurities can be heavily affected by variations in their density on the flux-surface. Using recently derived semi-analytic expressions for the transport of a collisional impurity species with high-$Z$ and flux-surface density-variation in the presence of a low-collisionality bulk ion species, we numerically optimize the impurity density-variation on the flux-surface to minimize the radial peaking-factor of the impurities. These optimized density-variations can notably reduce the peaking-factor in the Large Helical Device (LHD) case considered here, but have only a minor effect on the peaking-factor in a Wendelstein 7-X (W7-X) standard configuration case, where the peaking-factor already is negative in the core plasma. On the other hand, when the same procedure is used to find density-variations that maximize the peaking-factor, the peaking-factor is notably increased compared to the case with no density-variation. This highlights the potential importance of measuring and controlling these variations in experiments.

Keywords: fusion plasmas, collisional transport, stellarators, impurity transport

## I. INTRODUCTION

Highly-charged impurities can enter fusion plasmas from the walls of the vessel. In any magnetic-confinement fusion-reactor, these impurities must be prevented from accumulating in the core of the plasma, where they radiate strongly and lead to unsustainable energy losses.

Impurity accumulation is one of the major challenges in stellarators, where accumulation of impurities is often observed when the radial electric field points inwards[1–3] — which is the predicted operational regime for future reactors.

Such accumulation is also predicted theoretically, based on collisional transport calculations with simplified pitch-angle scattering collision operators. However, such simplified operators are not appropriate for treating highly-charged impurities with high collisionality[4]. When an appropriate collision operator is used, the radial transport of the heavy impurities becomes insensitive to the radial electric field[4–6]. Additionally, if the bulk ions are in a low-collisionality regime, impurity accumulation can be avoided by having large temperature gradients[4,6] – an effect known as *temperature screening*.

However, these results do not account for the tendency of highly-charged impurities to develop density-variations on the flux-surface[7–9]. Such variations occur when any plasma-species deviate from a flux-surface Maxwell-Boltzmann distribution, and are strongest for highly-charged species. When these variations are accounted for, the radial electric field again affects the transport of heavy-impurities[10,11]. In most scenarios, this leads to an accumulation of impurities[10,11], but there exist cases where the radial electric field is mildly beneficial:

In Ref. 10, where the density variation is due to electrostatic potential-variation from trapped-particles – calculated with the EUTERPE code – there exists a narrow range of inward radial-electric fields that lead to an outward impurity flux for one of the charge states ($Z = 24$, the lowest charge state investigated).

In Ref. 11, where a model of a localized flux-surface variation of impurities was considered, it was found that an inward radial-electric field can lead to weak outward transport if the amplitude of the localized variation is small.

Furthermore, the outward transport of carbon impurities can be enhanced by electrostatic potential-variations caused by fast, perpendicularly injected, neutral-beam particles[12].

Thus, it is in some cases possible for flux-surface density variations to reduce or prevent impurity accumulation. The purpose of the present work is to explore what beneficial impurity density variations look like, and how much they reduce the impurity accumulation. We do this by optimizing semi-analytical expressions for the impurity-transport coefficients from Ref. 11 with respect to the impurity density variation, to find variations that lead to the least (or most) impurity accumulation.

The remainder of this paper is organized as follows: in the next section, we present the mathematical formulation of the problem and analytic expressions for the impurity transport coefficients, radial flux and peaking-factor. In Sec. II A, we show how the impurity density variation is represented and optimized. In Sec. III, we discuss the results of such optimization applied to a Wendelstein 7-X (W7-X) and a Large Helical Device (LHD)

[a)] Electronic mail: bstefan@chalmers.se

case.

## II. MATHEMATICAL FORMULATION

In this section, we describe the radial transport of a highly-charged collisional impurity species (labeled "$z$") due to collisions with a bulk-ion species (labeled "$i$"). Specifically, we consider a *mixed-collisionality* regime[4] where the impurities are collisional and the bulk ions are in the $1/\nu$ regime. We here summarize results from Ref. 11.

The parallel momentum equation of a collisional impurity species is

$$T\nabla_\parallel n_z = -Zen_z\nabla_\parallel\Phi + R_{z\parallel}, \tag{1}$$

where $T$ is the impurity temperature, which is the same as the main-ion temperature $T_i = T$; $\nabla_\parallel$ denotes the gradient projected onto the magnetic field direction; $n_z$ is the impurity density, which varies along the flux-surface; $Ze$ is the charge of the impurity, $\Phi$ the electrostatic potential; and $R_{z\parallel}$ the parallel friction force. Under most conditions, the friction force is smaller than the other terms in this equation, which results in

$$n_z = N_z(r_N)\exp\left(-\frac{Ze\tilde{\Phi}}{T}\right), \tag{2}$$

where $r_N$ is a flux-surface label (in this paper, $r_N = \sqrt{\psi_\mathrm{t}/\psi_{\mathrm{t,LCFS}}}$, where $\psi_t$ is the toroidal flux and $\psi_{\mathrm{t,LCFS}}$ the toroidal flux at the last-closed flux-surface); $N_z$ is a flux-function known as the *pseudo-density*; and $\tilde{\Phi}$ is the deviation of $\Phi$ from its flux-surface average. The *Boltzmann-response* to the electrostatic potential, (2), commonly occurs as the collisional equilibrium density in confined plasma. If all species in the plasma would obey (2), quasi-neutrality would force $\Phi$ to be a flux-function, and all densities would be constant along the flux-surface. However, if any species deviate from (2), $\Phi$ will vary on the flux-surface, which can cause species with high $Z$ to develop significant density-variations on the flux-surface.

Assuming that (2) holds for the impurities – regardless of the mechanism that causes the $\Phi$ variation – the collisional radial transport of the impurities in the mixed-collisionality regime can be written as

$$\begin{aligned}\frac{\langle\boldsymbol{\Gamma}_z\cdot\nabla r_\mathrm{N}\rangle}{\langle n_z\rangle} =& -D_{N_z}[n_z]\frac{1}{Z}\frac{\mathrm{d}\ln N_z}{\mathrm{d}r_\mathrm{N}} + D_\Phi[n_z]\frac{e}{T}\frac{\mathrm{d}\langle\Phi\rangle}{\mathrm{d}r_\mathrm{N}}\\ &- D_{n_i}[n_z]\frac{\mathrm{d}\ln n_i}{\mathrm{d}r_\mathrm{N}} - D_{T_i}[n_z]\frac{\mathrm{d}\ln T}{\mathrm{d}r_\mathrm{N}},\end{aligned} \tag{3}$$

where the transport coefficients $D_X[n_z]$ depend on the impurity-variation on the flux-surface, as indicated by the square-brackets. Specifically,

$$\frac{D_{N_z}}{D} = \left\langle n_z w^2B^2\right\rangle - \left\langle n_z wB^2\right\rangle\frac{\left\langle wB^2\right\rangle}{\left\langle B^2\right\rangle} + \frac{\frac{\left\langle n_z wB^2\right\rangle}{\left\langle B^2\right\rangle}\left\langle\frac{B^2}{n_z}\right\rangle - \left\langle wB^2\right\rangle}{\left\langle\frac{B^2}{n_z}(1-c_4\alpha)\right\rangle}\left\langle(1-c_4\alpha)wB^2\right\rangle + \left\langle\frac{n_z|\nabla r_N|^2}{B^2}\right\rangle, \tag{4}$$

$$\frac{D_{n_i}}{D} = -\left\langle n_z wuB^2\right\rangle + \left\langle n_z wB^2\right\rangle\frac{\left\langle uB^2\right\rangle}{\left\langle B^2\right\rangle} - \frac{\frac{\left\langle n_z wB^2\right\rangle}{\left\langle B^2\right\rangle}\left\langle\frac{B^2}{n_z}\right\rangle - \left\langle wB^2\right\rangle}{\left\langle\frac{B^2}{n_z}(1-c_4\alpha)\right\rangle}\left(c_2 + \left\langle uB^2\right\rangle[c_1+1]\right) - \left\langle\frac{n_z|\nabla r_N|^2}{B^2}\right\rangle, \tag{5}$$

$$\begin{aligned}\frac{D_{T_i}}{D} =& \frac{1}{2}\left\langle n_z wuB^2\right\rangle - \frac{1}{2}\left\langle n_z wB^2\right\rangle\frac{\left\langle uB^2\right\rangle}{\left\langle B^2\right\rangle} - \frac{\frac{\left\langle n_z wB^2\right\rangle}{\left\langle B^2\right\rangle}\left\langle\frac{B^2}{n_z}\right\rangle - \left\langle wB^2\right\rangle}{\left\langle\frac{B^2}{n_z}(1-c_4\alpha)\right\rangle}\left(c_3 - \frac{3}{2}c_2 - \left\langle uB^2\right\rangle\left[c_1(\eta-1)+\frac{1}{2}\right]\right)\\ &+ \frac{1}{2}\left\langle\frac{n_z|\nabla r_N|^2}{B^2}\right\rangle,\end{aligned} \tag{6}$$

$$D_\Phi = -D_{n_i} - D_{N_z}, \tag{7}$$

where $D = \frac{m_i n_i T_i}{Ze^2\langle n_z\rangle n_z\tau_{iz}}$; $\alpha = Z^2 n_z/n_i$; $c_1$ to $c_4$ are flux-surface constants that depend on the magnetic geometry and $n_z$, defined in the Appendix A–C of Ref. 11; and

$$\boldsymbol{B}\cdot\nabla u = -\boldsymbol{B}\times\nabla\psi\cdot\nabla B^{-2}, \tag{8}$$

$$\boldsymbol{B}\cdot\nabla(n_z w) = -\boldsymbol{B}\times\nabla\psi\cdot\nabla(n_z B^{-2}). \tag{9}$$

The functions $u$, $w$ are evaluated numerically from the magnetic geometry and $n_z$, and the flux-surface constants $c_1$ to $c_4$ are integrated numerically.

From (3), we obtain the peaking-factor of $N_z$ by solving for the $-\frac{1}{Z}\frac{\mathrm{d}\ln N_z}{\mathrm{d}r_\mathrm{N}}$ that gives $\langle \mathbf{\Gamma}_z \cdot \nabla r_\mathrm{N}\rangle = 0$. Denoting this peaking-factor by $\mathcal{P}$, we obtain

$$\begin{aligned}\mathcal{P} =& -\frac{D_\Phi}{D_{N_z}}\frac{e}{T}\frac{\mathrm{d}\langle\Phi\rangle}{\mathrm{d}r_\mathrm{N}} + \frac{D_{n_i}}{D_{N_z}}\frac{\mathrm{d}\ln n_i}{\mathrm{d}r_\mathrm{N}} + \frac{D_{T_i}}{D_{N_z}}\frac{\mathrm{d}\ln T}{\mathrm{d}r_\mathrm{N}}\\ =& \left(1+\frac{D_{n_i}}{D_{N_z}}\right)\frac{e}{T}\frac{\mathrm{d}\langle\Phi\rangle}{\mathrm{d}r_\mathrm{N}} + \frac{D_{n_i}}{D_{N_z}}\frac{\mathrm{d}\ln n_i}{\mathrm{d}r_\mathrm{N}} + \frac{D_{T_i}}{D_{N_z}}\frac{\mathrm{d}\ln T}{\mathrm{d}r_\mathrm{N}}.\end{aligned} \tag{10}$$

To find the $n_z$ that minimizes impurity accumulation, we can minimize $\mathcal{P}$ which, according to (10), is equivalent to minimizing a weighted sum of $D_{n_i}/D_{N_z}$ and $D_{T_i}/D_{N_z}$. This picture can be further simplified, by noting that $D_{T_i} = -\frac{1}{2}D_{n_i}$ for $n_z$ that are constant on the flux-surface. In fact, here and in Ref. 11, we find $D_{T_i} \approx -0.5 D_{n_i}$ to within a few percent in many cases. With this approximation,

$$\mathcal{P} \approx \frac{e}{T}\frac{\mathrm{d}\langle\Phi\rangle}{\mathrm{d}r_\mathrm{N}} + \frac{D_{n_i}}{D_{N_z}}\left(\frac{e}{T}\frac{\mathrm{d}\langle\Phi\rangle}{\mathrm{d}r_\mathrm{N}} + \frac{\mathrm{d}\ln n_i}{\mathrm{d}r_\mathrm{N}} - 0.5\frac{\mathrm{d}\ln T}{\mathrm{d}r_\mathrm{N}}\right), \tag{11}$$

thus minimizing the peaking-factor becomes equivalent to either maximizing or minimizing $D_{n_i}/D_{N_z}$, depending on the sign of the expression in the parenthesis in (11). Thus, when this expression, which we denote by $X$, is far from zero, we expect the $n_z$ that optimizes the peaking-factor to be insensitive to the radial gradients – provided that the above approximation holds. Note that while the optimized $n_z$ is insensitive to the gradients, the actual value of the peaking-factor evaluated at this $n_z$ is sensitive to the gradients.

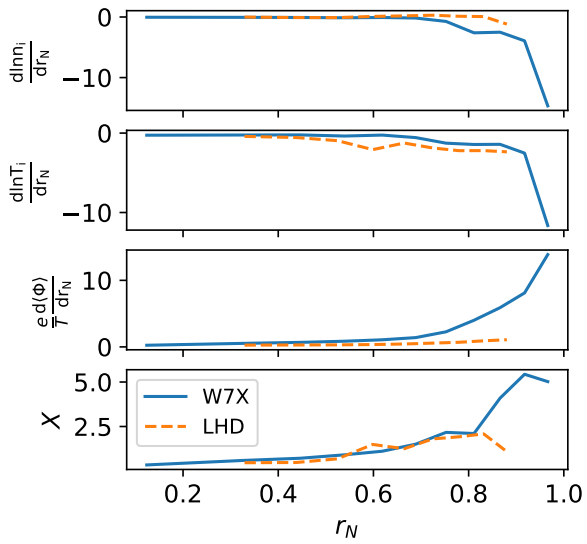


FIG. 1: Profile gradients of the W7-X (solid line) and LHD (dashed) case under consideration. Here $X$, refers to the expression in the parenthesis of (11). As $X$ is positive, minimizing the peaking-factor should correspond to minimizing $D_{n_i}/D_{N_z}$.

### A. Optimization

To avoid impurity accumulation, we seek to find an impurity density $n_z$ that minimizes (10). We restrict the problem to a finite number of degrees of freedom by expressing $n_z$ in terms of a truncated Fourier-expansion

$$\begin{aligned}n_z(\theta,\zeta) =& a_{00}f_{00}(\theta,\zeta) + \sum_{n=1}^{N}[a_{n0}f_{n0}(\theta,\zeta) + b_{n0}g_{n0}(\theta,\zeta)]\\ &+ \sum_{n=-N}^{N}\sum_{m=1}^{M}[a_{nm}f_{nm}(\theta,\zeta) + b_{nm}g_{nm}(\theta,\zeta)],\end{aligned} \tag{12}$$

where the basis functions

$$f_{nm}(\theta,\zeta) = 1 + \epsilon + \cos(m\theta - N_\mathrm{p}n\zeta), \tag{13}$$
$$g_{nm}(\theta,\zeta) = 1 + \epsilon + \sin(m\theta - N_\mathrm{p}n\zeta), \tag{14}$$

are chosen to be strictly positive ($\epsilon > 0$, here $\epsilon = 10^{-6}$) as the transport coefficients in (4)–(7) diverge for $n_z = 0$. Here, $\theta$ ($\zeta$) is the poloidal (toroidal) Boozer angle[13,14], with $N_\mathrm{p}$ the number of toroidal periods of the stellarator. Thus, we restrict ourselves to impurity densities that have the same discrete rotational symmetry as the magnetic field. To avoid unrealistically sharp variation in $n_z$ and to limit the dimensionality of the problem, we restrict ourselves to $N = M = 3$, which corresponds to 49 Fourier coefficients to optimize.

We eliminate one of the degrees of freedom, the $m = n = 0$ mode, by specifying $\langle n_z\rangle$ on the flux-surface. The state-vector of the problem thus consists of the 48 unconstrained Fourier-modes. We furthermore require that $n_z > d > 0$, which imposes a non-linear constraint on the Fourier-coefficients. The value of $d$ can be tuned to restrict $n_z$ to a realistic range of values; the effect of changing $d$ is investigated in appendix A.

The optimization proceeds from an initial state-vector from which we find a *local optimimum* by applying the gradient-based *method-of-moving-asymptotes*[15], as implemented in the python version of the non-linear optimization package NLopt[16].

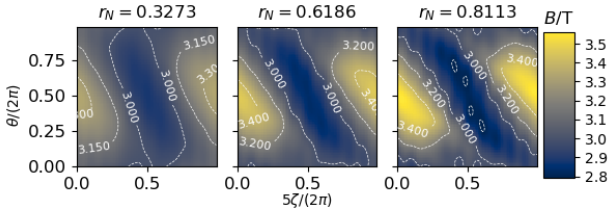


FIG. 2: Magnetic field strength $B$ for a W7-X standard configuration vacuum case.

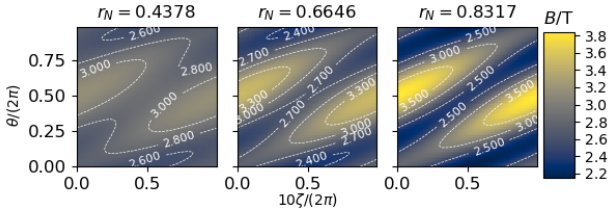


FIG. 3: Magnetic field strength $B$ for the LHD case[17,18].

## III. RESULTS

We optimize $n_z$ for a W7-X[1] and an LHD equilibrium[2], with the logarithmic gradients shown in Fig. 1 and magnetic geometry in Fig. 2 and Fig. 3. From the last subfigure in Fig. 1, we see that $(\frac{e}{T}\frac{\mathrm{d}\langle\Phi\rangle}{\mathrm{d}r_\mathrm{N}} + \frac{\mathrm{d}\ln n_i}{\mathrm{d}r_\mathrm{N}} - 0.5\frac{\mathrm{d}\ln T}{\mathrm{d}r_\mathrm{N}}) > 0$, which suggests that optimizing $n_z$ to minimize either the peaking-factor $\mathcal{P}$ or $D_{n_i}/D_{N_z}$ are approximately equivalent. The optimizations start from an initially homogeneous $n_z$, and we restrict the flux-surface variations to $n_z > 0.75\langle n_z\rangle$.

The results of such an optimization for three different radii are shown in Fig. 4 and Fig. 5, for the W7-X case and the LHD case, respectively. We see that the amplitude of the optimized $n_z$ tends to increase radially, as the amplitude of $B$ variations increase. For the W7-X case,

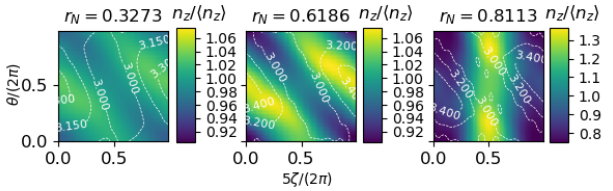


FIG. 4: $n_z$ optimized for minimum peaking-factor, for the W7-X cases in Fig. 2. The contours visualize the magnetic field at each flux-surface.

[1] W7-X standard configuration available at (Verified 2018-11-19) `https://github.com/landreman/sfincs/blob/master/equilibria/w7x-sc1.bc`

[2] LHD magnetic field taken from discharge #113208 at $t = 4.64\,\mathrm{s}$[17,18].

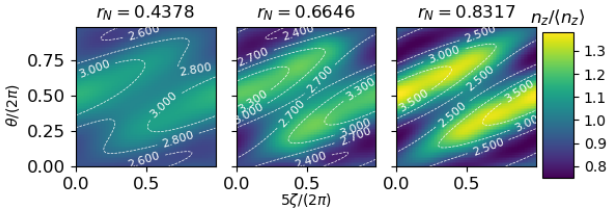


FIG. 5: Figure corresponding to Fig. 4, but for the LHD case.

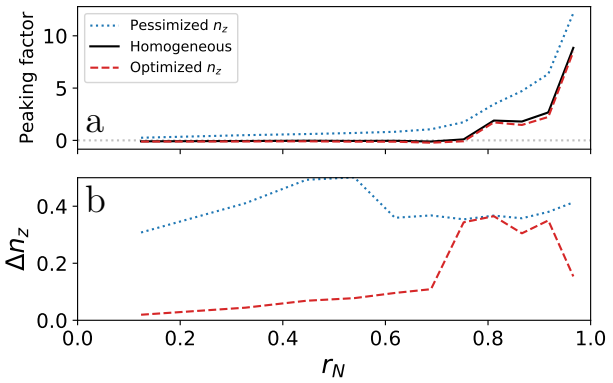


FIG. 6: **a:** Peaking-factor and a largest $n_z$ variations on the flux-surface for the W7-X case. **b:** the maximum deviation in $n_z/\langle n_z\rangle$.

the shape of the optimized $n_z$ are qualitatively different below and above $r_N \approx 0.7$. The corresponding potential variations are presented in appendix B. In both the LHD and W7-X for $r_N < 0.7$, the optimized $n_z$ are larger along the ridges of the maximum $B$, and peaking some distance away from the maximum value of $B$ – sometimes with a second peak at the maximum of $B$.

To evaluate the usefulness of targeting these optima, we need to know how much they reduce the peaking-factor. This is shown in Fig. 6a and Fig. 7a, for the W7-

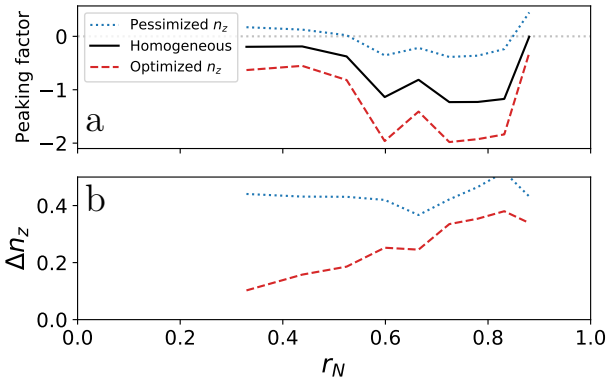


FIG. 7: Figure corresponding to Fig. 6, for the LHD case.

X and LHD cases. As seen in Fig. 6a, the optimization only slightly reduces the peaking-factor (red curve) compared to the homogeneous case (black) in the W7-X case. For the LHD case, the optimization has a larger effect, which suggests that the core impurity density could be reduced by modifying the impurity distribution on the flux-surface. In both cases, an unoptimized $n_z$ can result in a more peaked impurity profile, as seen from the pessimized curves in Fig. 6a and Fig. 7a – which were obtained by maximizing, rather than minimizing, the peaking-factor, where again we start from an initially homogeneous $n_z$. This appears consistent with the findings in Refs.[10,18,19], where the transport of impurities tends to be more inwards when the effect of $n_z$ variation (through the electrostatic potential variation) is accounted for. It may also be consistent with Ref. 12, where a beneficial effect of flux-surface variation is observed in simulations of the LHD.

In Fig. 6b and Fig. 7b, we show the maximum deviations of $n_z$ from the flux-surface value

$$\Delta n_z = \max_{\zeta,\theta} \left( \left| \frac{n_z(\zeta,\theta)}{\langle n_z \rangle} - 1 \right| \right), \tag{15}$$

which again illustrates that the amplitude of $n_z$ increases with radius, and that the nature of the optimized $n_z$ changes for $r_N \approx 0.7$ in the W7-X case. Despite the transition to a larger $n_z$ amplitude, there is no great change in the peaking-factor in this case, which shows that large $n_z$ variation can exist without severely impacting the peaking-factor. That being said, in both the W7-X and LHD case, the pessimized $n_z$ tends to have larger variations.

### A. Influence of small-amplitude modes

For the optimized $n_z$ to be reasonable targets in an experiment, they must be robust to small changes. We investigate this by considering how many of the 48 unconstrained Fourier modes actually contribute to lowering the peaking-factor.

We investigate this by zeroing out Fourier-coefficients below a threshold value in our representation of $n_z$, (12). The resulting change in peaking-factor and the number of retained unconstrained modes is shown in Fig. 8 and Fig. 9, for the W7-X and LHD case at two different radii, which are representative of the behaviour in the core and the edge. Note that the constrained $m = 0, n = 0$ cosine mode is always retained, and is set by the other modes to ensure that $\langle n_z \rangle$ is held constant. Also note the linear scale in the number of retained modes below 10 in Fig. 8 and Fig. 9, and the logarithmic scale when more than 10 modes are retained. For all cases, less than 10 modes actually contribute to visibly reducing the peaking-factor, as seen by the constant peaking-factor for low values of the zeroing-threshold. In fact, the sharpest increase in the peaking-factor occurs only when the last one or two unconstrained modes are zeroed out. In the core, this

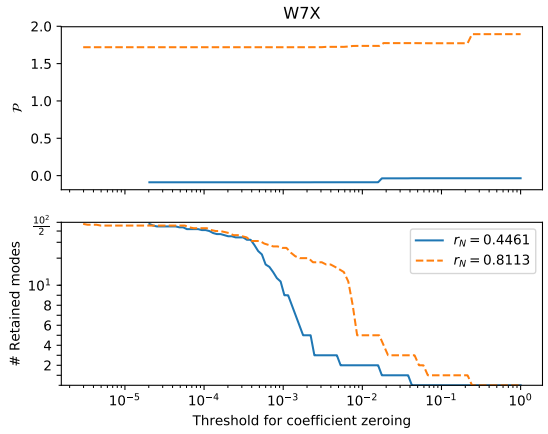


FIG. 8: The effects of zeroing out coefficients below a threshold value on the peaking-factor $\mathcal{P}$ in the W7-X case.

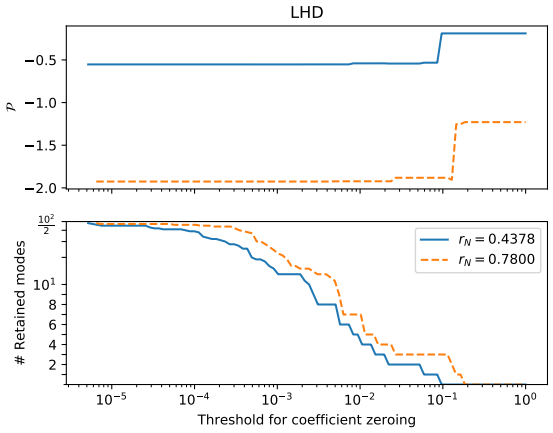


FIG. 9: Figure corresponding to Fig. 8 for the LHD case.

sharp increase occurs when the last (last two) unconstrained mode is zeroed, in the W7-X (LHD) case; in the edge, it occurs at two (one) modes in the W7-X (LHD) case. This implies that only one or two dominant unconstrained modes are needed for most of the optimization.

To illustrate which two modes are the dominant ones, we plot the amplitude of the relevant modes against radius in Fig. 10, alongside the constrained $m = 0, n = 0$ mode. From the W7-X subfigure in Fig. 10, we clearly see that the nature of the optimized $n_z$ changes for $0.75 < r_N < 0.95$, as previously observed, but it transitions back for $r_N \approx 0.95$. In the LHD case, the $m = 1, n = 0$ cosine mode is the dominant unconstrained mode at low $r_N$, but the $m = 2, n = 1$ cosine mode overtakes it at $r_N \approx 0.66$.

By restricting our attention only to the two dominant modes, we can visualize the entire optimization landscape to identify the globally optimal amplitudes for

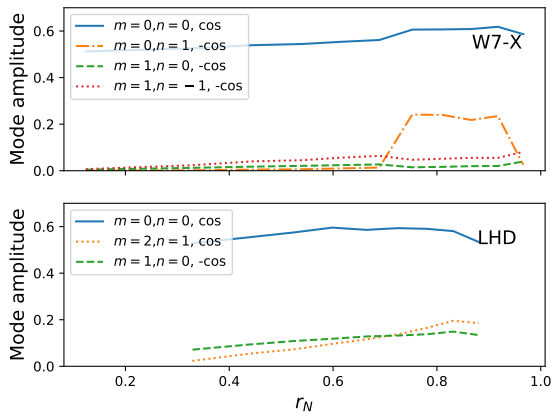


FIG. 10: Dominant modes for the different radii in the W7-X and LHD cases. Modes with negative amplitudes are marked with a "−" in the legend.

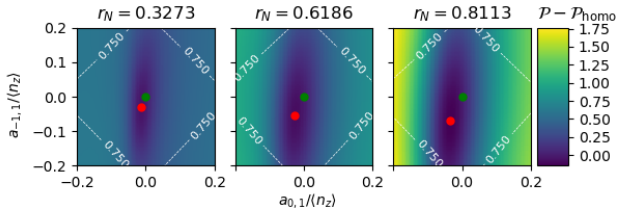


FIG. 11: The differential peaking-factor $\mathcal{P} - \mathcal{P}_{\text{homo}}$ at each point in an amplitude scan of the two dominant modes at low $r_N$ in the W7-X optimization. Note that these two modes are not dominant in the optimum found at $r_N$ around 0.8, see the W7-X subfigure of Fig. 10. The red dot indicates the location of the minimum, and the green dot a homogeneous $n_z$.

these modes. For this purpose, we perform a two dimensional scan in the amplitudes of the dominant modes for the W7-X and LHD cases. For the W7-X case, we restrict our attention to the two dominant modes at low $r_N$.

The peaking-factor for each point in the scan is illustrated in Fig. 11 and Fig. 12, for the W7-X and LHD case, respectively. The contour lines represent the limit imposed by the optimization requiring $n_z/\langle n_z \rangle > 0.75$.

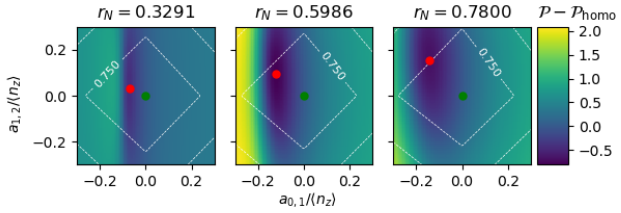


FIG. 12: A figure corresponding to Fig. 11, for the LHD case.

From these figures, we see that the optimum (red dot) tends to higher amplitudes for higher $r_N$, and also that it is the local optimum starting from an initially homogeneous $n_z$ (green dot). In both W7-X and LHD, the optimum is relatively narrow in the amplitude of the $m = 1, n = 0$ cosine mode (x-axis), but broadens for higher $r_N$. Regardless of how narrow the optimum is, it is always beneficial to have an $m = 1, n = 0$ cosine mode of moderate amplitude, compared to the homogeneous case, but the peaking-factor rapidly increases when the amplitude becomes too large. The peaking-factor is less sensitive to the amplitude of the other mode ($n = -1, m = 1$ in W7X, $n = 1, m = 2$ in LHD), but the minima in these broader basins nevertheless tend towards larger amplitudes at higher $r_N$. For the LHD case, the amplitude of the minima becomes sufficiently large to hit the $n_z > 0.75\langle n_z \rangle$ constraint, which we imposed to exclude unphysically large $n_z$ variation. This may indicate that this optimum $n_z$ may be difficult to achieve in reality. However, as there are still points with realistic amplitudes with peaking-factors lower than in the homogeneous case, $n_z$ optimization may still be worthwhile within the boundaries of realistic variations.

## IV. SUMMARY & CONCLUSIONS

We have performed numerical optimizations of the impurity density variation on the flux-surface, $n_z(\zeta, \theta)$, to minimize a semi-analytical expression for the impurity pseudo-density peaking-factor, valid in the *mixed-collisionality regime* with a collisional impurity and a low-collisionality bulk-ion species. In order to constrain $n_z$ to a realistic range of variations, we have only performed local optimizations of $n_z$ around a homogeneous initial value, using a gradient-based minimization method to minimize the peaking-factor. To further constrain $n_z$, we have imposed $n_z > 0.75\langle n_z \rangle$, as the optimization otherwise can produce unrealistically large $n_z$ variations on the flux-surface.

The results show that there is a potential to lower the collisional peaking-factor by controlling $n_z$ in the LHD case considered here, while the optimization in the W7-X case yields peaking-factors very close to those of a homogeneous $n_z$. On the other hand, we find that there are flux surface variations that lead to a notable increase in the impurity peaking factor in both the W7-X and LHD case.

As a conclusion, it may be worthwhile to experiment with $n_z$ variation to produce more hollow impurity profiles in LHD, as observed in Ref. 12. In particular, it appears that $m = 1, n = 0$ cosine modes of moderate amplitudes (up to $-0.05\langle n_z \rangle$ to $-0.2\langle n_z \rangle$, with larger amplitudes at larger radius) are beneficial in the case considered here. For the W7-X standard configuration, a homogeneous $n_z$ is close to optimal, and from this perspective, it may thus be wise to avoid $n_z$ variations. On the other hand, there exist $n_z$ variations with large ampli-

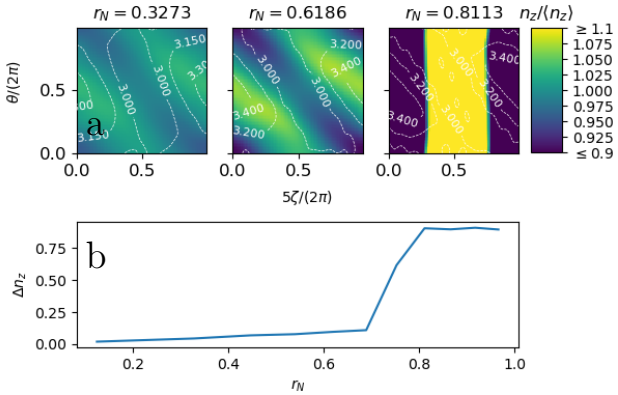


FIG. 13: **a:** $n_z$ optimized for minimum peaking-factor with $n_z > 0$, for the W7-X cases in Fig. 2. The contours visualize the magnetic field at each flux-surface. **b:** $\Delta n_z$ for each flux-surface.

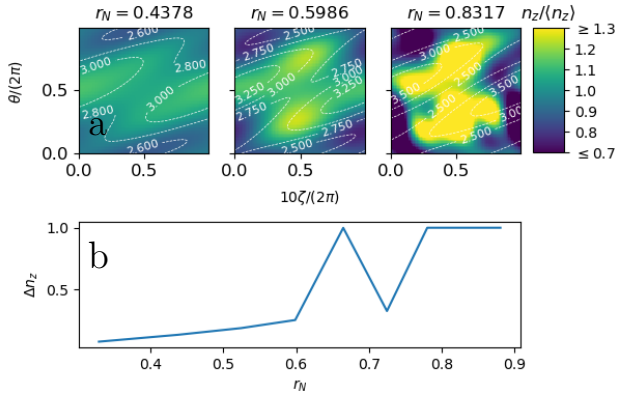


FIG. 14: Figure corresponding to Fig. 13, but for the LHD case.

tudes and slightly-better than homogeneous performance in W7-X, so $n_z$ variations are not intrinsically harmful.


## ACKNOWLEDGEMENT

This work has been carried out within the framework of the EUROfusion Consortium and has received funding from the Euratom research and training programme 2014-2018 under grant agreement No 633053. The views and opinions expressed herein do not necessarily reflect those of the European Commission. SB and IP were supported by the International Career Grant of Vetenskapsrådet (Dnr. 330-2014-6313) and IP by Marie Sklodowska Curie Actions, Cofund, Project INCA 600398. SB's trip to the 27th IAEA Fusion Energy Conference was supported by The Royal Society of Arts and Sciences in Gothenburg.


### Appendix A: Effects of changing the minimum $n_z$ value

In the bulk of this paper, we optimized $n_z$ given the constraint $n_z > 0.75\langle n_z \rangle$. Here, we show the effects of lifting that constraint, to demonstrate why such a constraint is necessary.

In Fig. 13a and Fig. 14a, we show the optimized $n_z$ obtained for the flux-surfaces in Fig. 2 and Fig. 3, by the optimization procedure described in Sec. II A starting from an initially homogeneous $n_z$ and only requiring $n_z > 0$ everywhere on the flux-surface.

From these figures, we see that the amplitude of the optimized $n_z$ initially increases with radii, while the shape remains similar. At some radius, the amplitudes "accessible" in the local optimization become large enough for the algorithm to find a new kind of local minimum, with radically different shape and unrealistically large amplitude. This occurs at $r_N \approx 0.70$ in the W7-X case, and at $r_N \approx 0.75$ in the LHD case – although a similar optimum is also found at $r_N = 0.66$ in this LHD case, as seen from Fig. 14b.

Thus, without specifying a lowest allowed value for $n_z$, even optimizations starting from a homogeneous initial $n_z$ cannot be guaranteed to display reasonable $n_z$ variations. The shape of the optima found at the outer radii in Fig. 13a is in fact very similar to a "global" optimum obtained by stochastic optimization where several initial $n_z$ are randomly generated and the lowest local optimum resulting from performing local optimization from these initial $n_z$'s is taken as an upper bound for the global minimum. The result of this process for $r_N = 0.6$ in W7-X is shown in Fig. 15. The situation in the W7-X case may thus be illustrated as in Fig. 16, where there always exist local minima unrealistically far from a homogeneous $n_z$ that are more optimal than those obtained from starting the local optimization at a homogeneous $n_z$.

This is the reason for optimizing on a more restrictive function-space, for example by specifying $n_z > d$ for some $d$. A better approach would be to restrict $n_z$ to a function-space of "reasonable" impurity density variations based on the physical modeling of the phenomena causing the flux-surface variation, but this is outside the scope of this work.

### Appendix B: Corresponding potential variation

In this work, we calculate $n_z$ that optimize the impurity peaking-factor, with little regard for the physical mechanisms that set $n_z$. However, physics-based calculation of $n_z$ often calculate flux-surface variation of the electrostatic potential, from which $n_z$ is obtained through (2). To connect our results to previous theoretical studies, we thus invert (2) to obtain $\tilde{\Phi}$'s corresponding to our optimized $n_z$

$$\frac{Ze\tilde{\Phi}}{T} = -\log n_z + C, \tag{B1}$$

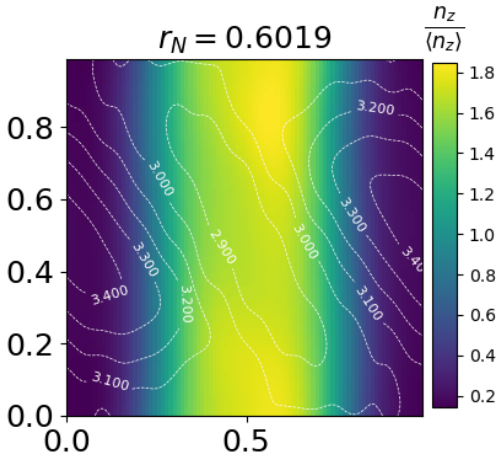


FIG. 15: Optimized $n_z$ resulting from stochastic optimization in the W7-X case at $r_N = 0.6$.

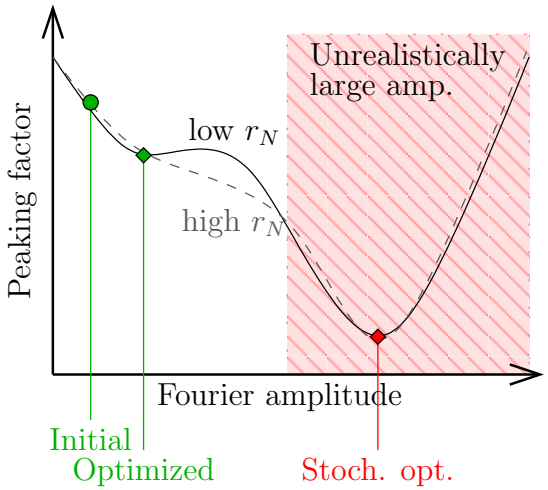


FIG. 16: Illustration of the local optimization landscape in the W7-X case, for two different radii. At higher $r_N$, a local optimizer starting at a uniform $n_z$ finds an optimum that was inaccessible but existed at lower $r_N$; as revealed by the stochastic optimization. The differences in Peaking-factor is here exaggerated for the purpose of illustration.

where $C$ is a constant calculated to make $\langle \tilde{\Phi} \rangle = 0$. The resulting $Ze\tilde{\Phi}/T$ for the W7-X and LHD cases are displayed in Fig. 17 and Fig. 18.

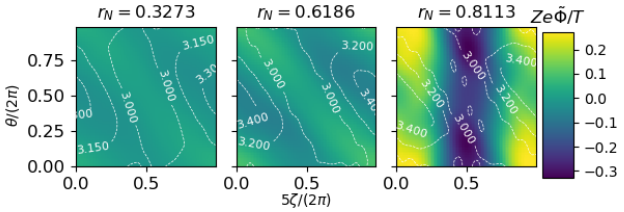


FIG. 17: $\tilde{\Phi}$ corresponding to the W7-X $n_z$ in Fig. 4.

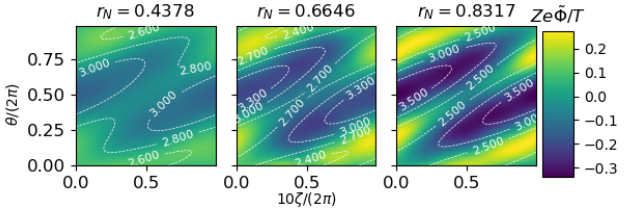


FIG. 18: $\tilde{\Phi}$ corresponding to the LHD $n_z$ in Fig. 5.


[1] L. Giannone, J. Baldzuhn, R. Burhenn, P. Grigull, U. Stroth, F. Wagner, R. Brakel, C. Fuchs, H. J. Hartfuss, K. McCormick, A. Weller, C. Wendland, N. Team, E. Team, W.-A. Team, K. Itoh, and S.-I. Itoh, "Physics of the density limit in the w7-as stellarator," Plasma Physics and Controlled Fusion **42**, 603 (2000).

[2] Y. Nakamura, Y. Takeiri, B. J. Peterson, S. Muto, K. Ida, H. Funaba, M. Yokoyama, K. Narihara, Y. Nagayama, S. Inagaki, T. Tokuzawa, S. Morita, M. Goto, K. Sato, M. Osakabe, S. Masuzaki, H. Suzuki, R. Kumazawa, T. Mutoh, T. Shimozuma, M. Sato, N. Noda, K. Kawahata, N. Ohyabu, O. Motojima, and L. E. Group, "Impurity behaviour in lhd long pulse discharges," Plasma Physics and Controlled Fusion **44**, 2121 (2002).

[3] R. Burhenn, Y. Feng, K. Ida, H. Maassberg, K. McCarthy, D. Kalinina, M. Kobayashi, S. Morita, Y. Nakamura, H. Nozato, S. Okamura, S. Sudo, C. Suzuki, N. Tamura, A. Weller, M. Yoshinuma, and B. Zurro, "On impurity handling in high performance stellarator/heliotron plasmas," Nuclear Fusion **49**, 065005 (2009).

[4] P. Helander, S. L. Newton, A. Mollén, and H. M. Smith, "Impurity transport in a mixed-collisionality stellarator plasma," Phys. Rev. Lett. **118**, 155002 (2017).

[5] S. Braun and P. Helander, "Pfirsch-Schlüter impurity transport in stellarators," Physics of Plasmas **17**, 072514 (2010), https://doi.org/10.1063/1.3458901.

[6] S. L. Newton, P. Helander, A. Mollén, and H. M. Smith, "Impurity transport and bulk ion flow in a mixed collisionality stellarator plasma," Journal of Plasma Physics **83**, 905830505 (2017).

[7] P. Helander, "Bifurcated neoclassical particle transport," Physics of Plasmas **5**, 3999–4004 (1998), http://dx.doi.org/10.1063/1.873121.

[8] T. Fülöp and P. Helander, "Nonlinear neoclassical transport in a rotating impure plasma with large gradients," Physics of Plasmas **6**, 3066–3075 (1999), http://dx.doi.org/10.1063/1.873593.

[9] C. Angioni and P. Helander, "Neoclassical transport of heavy impurities with poloidally asymmetric density distribution in tokamaks," Plasma Physics and Controlled Fusion **56**, 124001 (2014).

[10] I. Calvo, F. I. Parra, J. L. Velasco, J. A. Alonso, and J. Garcia-Regaa, "Stellarator impurity flux driven by electric fields tangent to magnetic surfaces," Nuclear Fusion **58**, 124005 (2018).

[11] S. Buller, H. M. Smith, P. Helander, A. Mollén, S. L. Newton, and I. Pusztai, "Collisional transport of impurities with flux-surface varying density in stellarators," Journal of Plasma Physics **84**, 905840409 (2018).

[12] H. Yamaguchi and S. Murakami, "Simulation study of electrostatic potential generated by NBI and its effect on the neoclassical transport of carbon impurity ions in LHD," IAEA FEC 2018 preprints (2018).

[13] A. H. Boozer, "Plasma equilibrium with rational magnetic surfaces," The Physics of Fluids **24**, 1999–2003 (1981), https://aip.scitation.org/doi/pdf/10.1063/1.863297.

[14] P. Helander, "Theory of plasma confinement in non-axisymmetric magnetic fields," Reports on Progress in Physics **77**, 087001 (2014).

[15]K. Svanberg, "The method of moving asymptotesa new method for structural optimization," International Journal for Numerical Methods in Engineering **24**, 359–373 (1987), https://onlinelibrary.wiley.com/doi/pdf/10.1002/nme.1620240207.
[16]S. G. Johnson, "The nlopt nonlinear-optimization package," .
[17]J. Velasco, I. Calvo, S. Satake, A. Alonso, M. Nunami, M. Yokoyama, M. Sato, T. Estrada, J. Fontdecaba, M. Liniers, K. McCarthy, F. Medina, B. P. V. Milligen, M. Ochando, F. Parra, H. Sugama, A. Zhezhera, The LHD Experimental Team, and The TJ-II Team, "Moderation of neoclassical impurity accumulation in high temperature plasmas of helical devices," Nuclear Fusion **57**, 016016 (2017).
[18]A. Mollén, M. Landreman, H. M. Smith, J. M. García-Regaña, and M. Nunami, "Flux-surface variations of the electrostatic potential in stellarators: impact on the radial electric field and neoclassical impurity transport," Plasma Physics and Controlled Fusion **60**, 084001 (2018).
[19]J. García-Regaña, C. Beidler, R. Kleiber, P. Helander, A. Mollén, J. Alonso, M. Landreman, H. Maaßberg, H. Smith, Y. Turkin, and J. Velasco, "Electrostatic potential variation on the flux surface and its impact on impurity transport," Nuclear Fusion **57**, 056004 (2017).